Discovery and Preliminary Characterization of a Third Interstellar Object: 3I/ATLAS

Darryl Z. Seligman [1,*] Marco Micheli [2] Davide Farnocchia [3] Larry Denneau [4] John W. Noonan [5]
Henry H. Hsieh [6] Toni Santana-Ros [7,8] John Tonry [4] Katie Auchettl [9,10] Luca Conversi [2]
Maxime Devogèle [2] Laura Faggioli [2] Adina D. Feinstein [1,†] Marco Fenucci [2] Marin Ferrais [11]
Tessa Frincke [1] Olivier R. Hainaut [12] Kyle Hart [4] Andrew Hoffman [4] Carrie E. Holt [13]
Willem B. Hoogendam [4,‡] Mark E. Huber [4] Emmanuel Jehin [14] Theodore Kareta [15,16]
Jacqueline V. Keane [17] Michael S. P. Kelley [18] Tim Lister [13] Kathleen Mandt [19] Dušan Marčeta [20]
Karen J. Meech [4] Mohamed Amine Miftah [21,22] Marvin Morgan [23] Francisco Ocaña [2]
Eloy Peña-Asensio [24] Benjamin J. Shappee [4] Robert J. Siverd [4] Aster G. Taylor [25,§]
Michael A. Tucker [26,27] Richard Wainscoat [4] Robert Weryk [28] James J. Wray [29]
Atsuhiro Yaginuma [30] Bin Yang [31] Quanzhi Ye (叶泉志) [18,32] and Qicheng Zhang [16]

[1] Department of Physics and Astronomy, Michigan State University, East Lansing, MI 48824, USA
[2] ESA NEO Coordination Centre, Largo Galileo Galilei 1, I-00044 Frascati (RM), Italy
[3] Jet Propulsion Laboratory, California Institute of Technology, 4800 Oak Grove Dr., Pasadena, CA 91109, USA
[4] Institute for Astronomy, University of Hawaii, 2680 Woodlawn Drive, Honolulu, HI 96822, USA
[5] Department of Physics, Auburn University, Edmund C. Leach Science Center, Auburn, 36849, AL, USA
[6] Planetary Science Institute, 1700 East Fort Lowell Rd., Suite 106, Tucson, AZ 85719, USA
[7] Departamento de Física, Ingeniería de Sistemas y Teoría de la Señal, Universidad de Alicante, Carr. San Vicente del Raspeig, s/n,
03690 San Vicente del Raspeig, Alicante, Spain
[8] Institut de Ciències del Cosmos (ICCUB), Universitat de Barcelona (UB), c. Martí Franquès, 1, 08028 Barcelona, Catalonia, Spain
[9] School of Physics, University of Melbourne, Parkville, VIC 3010, Australia
[10] Department of Astronomy and Astrophysics, University of California, Santa Cruz, CA 93105, USA
[11] Florida Space Institute, University of Central Florida, 12354 Research Parkway, Orlando, FL 32828, USA
[12] European Southern Observatory, Karl-Schwarzschild-St. 2, 85748 Garching-bei-München, Germany
[13] Las Cumbres Observatory, 6740 Cortona Drive, Suite 102, Goleta, CA 93117, USA
[14] Space sciences, Technologies & Astrophysics Research (STAR) Institute Université de Liége 4000 Liege, Belgium
[15] Dept. of Astrophysics and Planetary Science, Villanova University, Villanova, PA, USA
[16] Lowell Observatory, 1400 W Mars Hill Rd, Flagstaff, AZ 86001, USA
[17] U.S. National Science Foundation, 2415 Eisenhower Avenue, Alexandria, VA 22314, USA
[18] Department of Astronomy, University of Maryland, College Park, MD 20742-0001, USA
[19] NASA Goddard Space Flight Center, Greenbelt, MD, 20771, USA
[20] Department of Astronomy, Faculty of Mathematics, University of Belgrade, Serbia
[21] Space sciences, Technologies & Astrophysics Research (STAR) Institute Université de Liéege 4000 Liege, Belgium
[22] Cadi Ayyad University (UCA), Oukaimeden Observatory (OUCA), Faculté des Sciences Semlalia (FSSM), High Energy Physics,
Astrophysics and Geoscience Laboratory (LPHEAG), Marrakech, Morocco
[23] Department of Physics, University of California, Santa Barbara, Santa Barbara, CA 93106, USA
[24] Department of Aerospace Science and Technology, Politecnico di Milano, Via La Masa 34, 20156 Milano, Italy
[25] Dept. of Astronomy, University of Michigan, Ann Arbor, MI 48109, USA
[26] Center for Cosmology & Astroparticle Physics, The Ohio State University, Columbus, OH, USA
[27] Department of Astronomy, The Ohio State University, Columbus, OH, USA
[28] Department of Physics and Astronomy, The University of Western Ontario, 1151 Richmond Street, London, ON N6A 3K7, Canada
[29] School of Earth and Atmospheric Sciences, Georgia Institute of Technology, 311 Ferst Drive, Atlanta, GA 30332, USA
[30] Dept. of Physics and Astronomy, Michigan State University, East Lansing, MI 48824, USA
[31] Instituto de Estudios Astrofísicos, Facultad de Ingeniería y Ciencias, Universidad Diego Portales, Santiago, Chile
[32] Center for Space Physics, Boston University, 725 Commonwealth Ave, Boston, MA 02215, USA

ABSTRACT

We report initial observations aimed at the characterization of a third interstellar object candidate.
This object, 3I/ATLAS or C/2025 N1 (ATLAS), was discovered on 2025 July 1 UT and has an orbital

Email: dzs@msu.edu

eccentricity of $e \sim 6.1$, perihelion of $q \sim 1.36$ au, inclination of $\sim 175°$, and hyperbolic velocity of $V_\infty \sim 58$ km s^{-1}. We report deep stacked images obtained using the Canada-France-Hawaii Telescope and the Very Large Telescope that resolve a compact coma. Using images obtained from several smaller ground-based telescopes, we find minimal light curve variation for the object over a ~ 4 day time span. The visible/near-infrared spectral slope of the object is 17.1±0.2 %/100 nm, comparable to other interstellar objects and primitive solar system small bodies (comets and D-type asteroids), although this result is likely affected by some coma contamination. 3I/ATLAS will be observable through early September 2025, then unobservable by Earth-based observatories near perihelion due to low solar elongation. It will be observable again from the ground in late November 2025. Although this limitation unfortunately prohibits detailed Earth-based observations at perihelion when the activity of 3I/ATLAS is likely to peak, spacecraft at Mars could be used to make valuable observations at this time. Additional photometric, spectroscopic, and polarimetric monitoring of 3I/ATLAS by ground- and space-based telescopes, and possibly spacecraft based at Mars, are highly encouraged for characterizing 3I/ATLAS's rotational light curve, activity evolution, nongravitational acceleration, and compositional indicators of formation conditions.

1. INTRODUCTION

The first two interstellar objects identified traversing the inner Solar System, 1I/'Oumuamua (Williams et al. 2017) and 2I/Borisov (Borisov et al. 2019), were discovered in 2017 and 2019, respectively. It has been suggested that interstellar objects formed in protostellar disks (Fitzsimmons et al. 2024) or the cores of giant molecular clouds (Hsieh et al. 2021). Although there is little hope of identifying the exact home system for a given interstellar object (Hallatt & Wiegert 2020), they provide the best opportunity to directly measure the properties of small bodies that formed outside of our solar system.

These first interstellar objects displayed divergent properties. For one, 1I/'Oumuamua displayed no visible activity (Meech et al. 2017; Ye et al. 2017; Jewitt et al. 2017; Trilling et al. 2018), yet nongravitational acceleration was detected in its trajectory at the $\sim 30\sigma$ level (Micheli et al. 2018). Meanwhile, 2I/Borisov displayed clear outgassing and dust ejection activity (Jewitt & Luu 2019; Fitzsimmons et al. 2019; Bolin et al. 2020; Ye et al. 2020; McKay et al. 2020; Guzik et al. 2020; Hui et al. 2020; Kim et al. 2020; Cremonese et al. 2020; Yang et al. 2021). The excess velocity of 1I/'Oumuamua and 2I/Borisov also differed significantly. These objects had velocities of $V_\infty \sim 26$ km s^{-1} and $V_\infty \sim 32$ km s^{-1} respectively, which approximately correspond to ages of $\sim 10^2$ and $\sim 10^3$ Myr (Mamajek 2017; Gaidos et al.

* NSF Astronomy and Astrophysics Postdoctoral Fellow
† NHFP Sagan Fellow
‡ NSF Graduate Research Fellow
§ Fannie and John Hertz Foundation Fellow

2017; Feng & Jones 2018; Almeida-Fernandes & Rocha-Pinto 2018; Hallatt & Wiegert 2020; Hsieh et al. 2021). In addition, 1I/'Oumuamua displayed brightness variations of ~ 3.5 magnitudes corresponding to an extreme oblate $6 : 6 : 1$ geometry (Meech et al. 2017; Knight et al. 2017; Bolin et al. 2018; Fraser et al. 2018; Belton et al. 2018; Mashchenko 2019; Taylor et al. 2023) and had a moderately red reflectance spectrum (Meech et al. 2017; Fitzsimmons et al. 2018; Ye et al. 2017).

These divergent properties led to a variety of hypotheses regarding the provenance of the population. Although 2I/Borisov's coma was found to contain volatile species typically seen in comets (Opitom et al. 2019; Kareta et al. 2020; Lin et al. 2020; Bannister et al. 2020; Xing et al. 2020; Bagnulo et al. 2021; Aravind et al. 2021), it had a high enrichment of CO relative to H_2O (Bodewits et al. 2020; Cordiner et al. 2020). These ratios differentiate its composition from most solar system comets, which are typically rich in H_2O and contain CO between 1–15% relative to water (Biver et al. 2024).

1I/'Oumuamua's lack of visible activity despite its nongravitational acceleration has led to a variety of hypothesized origins. Micheli et al. (2018) noted that for radiation pressure to cause the nongravitational acceleration, the object must either have an exceptionally low density or an extreme geometry. Such a density is a possible byproduct of diffusion-limited aggregation formation processes in the outskirts of a protostellar disk (Moro-Martín 2019). Somewhat counterintuitively, it has also been demonstrated that such hypothetical structures bound together by weak van der Waals forces could survive tidal disruption from the Solar gravity (Flekkøy et al. 2019). It was also hypothesized that

such a fractal aggregate could form in the coma of an undiscovered parent interstellar comet (Luu et al. 2020).

Alternatively, 1I/'Oumuamua could have been outgassing volatiles with low levels of dust production, rendering it photometrically inactive in all extant observations (Micheli et al. 2018; Sekanina 2019; Seligman & Laughlin 2020; Levine et al. 2021; Levine & Laughlin 2021; Desch & Jackson 2021; Jackson & Desch 2021; Desch & Jackson 2022; Bergner & Seligman 2023). This argument has been recently bolstered; since the discovery of 1I/'Oumuamua, a series of photometrically inactive near-Earth objects (NEOs) have been reported to have significant comet-like nongravitational accelerations (Farnocchia et al. 2023; Seligman et al. 2023, 2024). These objects imply that 1I/'Oumuamua-like nongravitational accelerations may be more common than previously thought (Taylor et al. 2024). Regardless, our understanding of interstellar objects is incomplete. See Fitzsimmons et al. (2024), Seligman & Moro-Martín (2023), Jewitt & Seligman (2023), and Moro-Martín (2022) for recent reviews on this topic.

In this paper, we report early observations of 3I/ATLAS, the third interstellar object to be discovered after 1I/'Oumuamua and 2I/Borisov, to help inform and coordinate follow-up observations.

2. DISCOVERY AND HYPERBOLIC ORBIT CHARACTERIZATION

2.1. *Discovery*

3I/ATLAS was discovered through the robotic observing schedule from ATLAS Chile (Tonry et al. 2018a) on 2025 July 1 and given the internal designation A11pl3Z[33] (see Figure 1). The discovery tracklet was immediately submitted to the Minor Planet Center (MPC). Follow-up observations were then conducted by ATLAS in Hawai'i, Sutherland, and the Canary Islands, along with dozens of other observatories worldwide. The discovery was made by ATLAS largely because the object was located in the Galactic plane — a region typically avoided by more sensitive surveys, such as Pan-STARRS and the Catalina Sky Survey.

Six hours after the initial detection by ATLAS on 2025 July 1, prediscovery detections from 2025 June 28–29 were identified in Zwicky Transient Facility (ZTF; Bellm et al. 2019; Graham et al. 2019) survey data, extending the orbital arc from 3.3 hours to 3 days. The new 3-day arc suggested a strongly hyperbolic orbit and prompted speculation on community mailing lists that the object might be interstellar. Later on the early hours of 2025
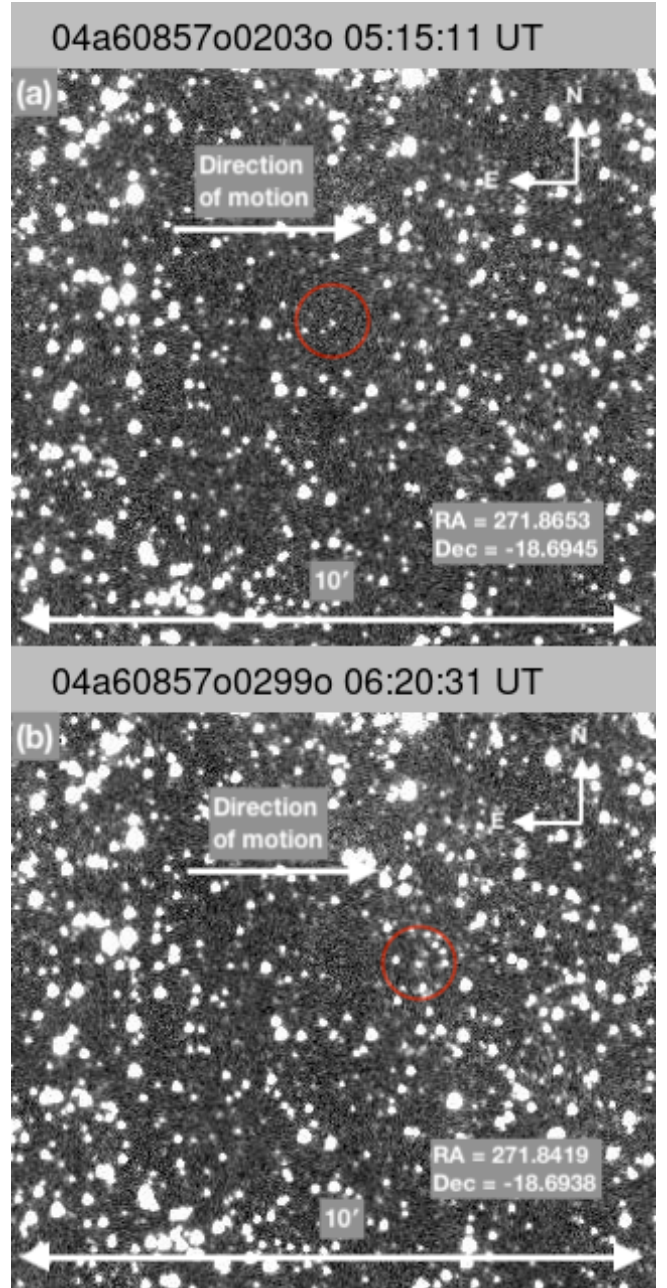

Figure 1. Cutout images from the first and fourth discovery observations of 3I/ATLAS from the ATLAS Chile, spanning approximately one hour. 3I/ATLAS is moving at 0.49 deg/day against the stellar background. The cardinal directions and direction of motion are indicated with arrows, and 3I/ATLAS is identified within the red circle. (a) Un-background subtracted image from 05:15:11 UT; (b) Un-background subtracted image from 06:20:31 UT.

July 2 UT, additional prediscovery pairs and triplets were identified in ATLAS data from five days earlier by S. Deen and later refined and resubmitted to the MPC by the ATLAS team. More prediscovery detections from

---

[33] https://www.minorplanetcenter.net/mpec/K25/K25N12.html
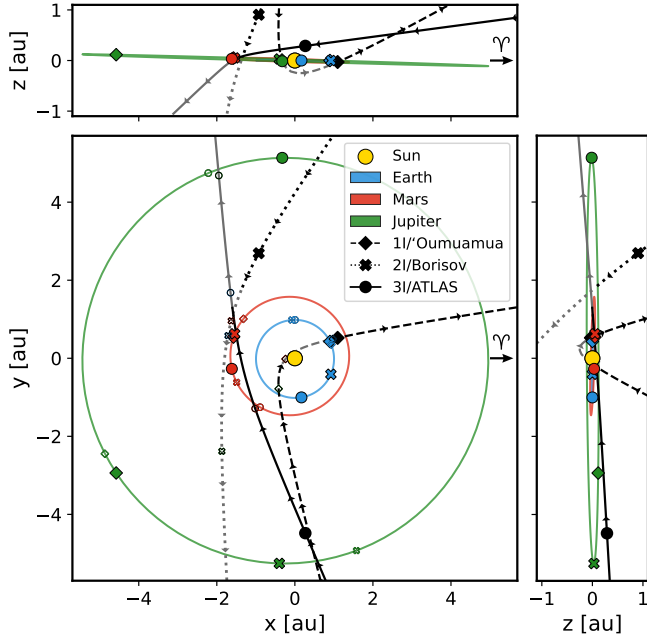
Figure 2. Heliocentric orbit (ECLIPJ2000) of 1I/'Oumuamua, 2I/Borisov, 3I/ATLAS, Earth, Mars, and Jupiter. Black lines represent the orbital path of each object; gray lines represent when the interstellar object is below-ecliptic. We highlight the location of the Sun (yellow) and the orbital paths of Earth (blue), Mars (red), and Jupiter (green). Large filled markers represent where the respective colored planet was when the interstellar object was discovered. Small unfilled markers represent where the planet will be at the interstellar object's closest approach. Arrows point along the motion direction. The vernal equinox is indicated to the right.

ZTF, dating back to 2025 June 14[34], were also identified and submitted.

At the time of discovery in the ATLAS data, the object had a magnitude 17.7–17.9 in the *o*-band filter (see Figure 1), and was at a heliocentric distance of $r = 4.51$ au and a geocentric distance of $\Delta = 3.50$ au.

2.2. *Orbit Characterization*

As of the early hours of 2025 July 2, the initial discovery and prediscovery arc, covering a total of about 18 days, was sufficient to confirm the large eccentricity and, consequently, hyperbolic nature of the object's orbit. As soon as the unusual nature of the object became evident, a large number of follow-up observations were obtained on 2025 July 2 by various observatories, leading to additional orbit refinement.

---

[34] Another batch of ZTF prediscovery detections, dating back to 2025 May 22, were later submitted and published in MPEC 2025-N51 (https://minorplanetcenter.net/mpec/K25/K25N51.html).

Table 1. Initial orbit of 3I/ATLAS, computed using astrometry from 2025 May 22 to 2025 July 6. Heliocentric orbital elements at the epoch of 2025 July 3 TDB.

Orbital element	Value $\pm$ 1σ
Perihelion distance q [au]	1.3558541 ± 0.0019855
Eccentricity e	6.1329072 ± 0.0162018
Inclination i [°]	175.11239 ± 0.00089
Longitude of ascending node Ω [°]	322.14485 ± 0.01806
Argument of perihelion ω [°]	128.01038 ± 0.02340
Time of perihelion T_P [MJD, TDB]	60977.51085 ± 0.04078

Within our team, we first acquired 31 unfiltered 163 s exposures starting at 06:34 2025 UT July 2 spanning a total of 93 minutes using the European Space Agency's (ESA) 0.56-meter Test Bed Telescope (TBT; MPC code W57) at La Silla Observatory in Chile, which has a field of view of 2.5° × 2.5°. The telescope is fully devoted to NEO survey and follow-up observations, and can be interrupted at any time for high-profile targets.

We also obtained detections with one of the Las Cumbres Observatory (LCO) 0.35-meter telescopes on Haleakala (MPC code T03) and with the 2.0-meter Faulkes Telescope North (FTN; MPC code F65) and South (FTS, MPC code E10) between 2025 July 2 and July 4, which provided astrometric measurements with an astrometric accuracy better than $\pm0''.25$.

A successful DDT request to the European Southern Observatory's (ESO) 8.2-meter Very Large Telescope (VLT), submitted on the same day and quickly approved, also allowed our team to obtain good-seeing images of the object on 2025 July 4. High-precision astrometry (better than $\pm0''.1$) was extracted from this dataset, using an extrapolation to zero aperture to ensure correction for possible asymmetries in the inner coma of the object.

Our best estimate of the heliocentric orbital elements of the object, at the time of submission of this paper, is listed in Table 1. In Figure 2, we show the orbit of the object in comparison to previously discovered interstellar objects.

From the current heliocentric orbit, it is possible to infer the incoming trajectory of the object before it entered our Solar System. The eccentricity of the object's orbit with respect to the Solar System barycenter, computed before interacting with our planetary system, can be extrapolated as $e_b = 6.144 \pm 0.016$. This value, together with an incoming pericenter distance of $q_b = (1.3611 \pm 0.0020)$ au, results in an incoming velocity $v_\infty = (57.942 \pm 0.049)$ km s^{-1}, from an asymptote directed towards a Right Ascension of $\sim 295°$ and a

Declination of $\sim -19°$, in the constellation of Sagittarius and not far from the Galactic Center.

3I/ATLAS is predicted to approach within 0.19 au of Mars on 2025 October 3.

3. OBSERVATIONAL ANALYSIS

3.1. *Activity*

Given the stark difference in visible activity levels between 1I/'Oumuamua and 2I/Borisov (Section 1), a high priority for initial observational analysis for 3I/ATLAS was determining whether it was active or not. With this in mind, we obtained three 60 s non-sidereally guided *gri*-band images with the MegaCam wide-field mosaic imager (Boulade et al. 2003) on the 3.6-meter Canada-France-Hawaii Telescope (CFHT, MPC code T14) on 2025 July 2 to search for faint cometary activity. The highest-quality image had typical stellar FHWMs of $0.''72 \pm 0.''05$ measured perpendicular to the direction of trailing, while the object had a FWHM of $1.''29 \pm 0.''02$. The magnitude in a $5''$ radius aperture was 17.2 in the *Gaia* DR2 G band after three background stars were masked, although the field was crowded, so we consider this measurement to be unreliable. Figure 3a shows the stacked composite image of these data in which faint activity is visible.

On 2025 July 4, fifteen 10 s *R*-band images were acquired using the FORS2 instrument on the 8.2-meter Unit Telescope 1 of the European Southern Observatory Very Large Telescope (VLT) on Paranal, Chile. The measured image quality was $0.''6$ FWHM. However, the object had a FWHM of $1.''49 \times 1.''29$ with the asymmetric elongation pointing to position angle 277° from North to East, where the coma can be seen out to $3.''5$. A composite image of these data is shown in Figure 3b. The photometric profile of the object (Figure 4) shows an excess extending over $4''$ compared to that of field stars.

As noted in Section 2, g'- and r'-band precovery data from ZTF were published in MPEC 2025-N51 following these observations. This included photometry dating back to 2025 May 22. These data mostly consisted of single g'- or r'-band detections on each night, but included pairs of g' and r'-band detections on 2025 May 22 and June 18. We compute inferred V-band absolute magnitude from these data assuming a standard asteroidal phase function (Bowell et al. 1989) assuming $G = 0.15$ and solar colors (Jordi et al. 2006; Holmberg et al. 2006). We use this to present a secular light curve in Figure 5. The computed absolute magnitudes are relatively constant between 2025 May 22 and June 14 (during which the object ranged between heliocentric distances of $r = 5.8$ au to $r = 5.1$ au). The secular light curve has a median value of $H_V = 12.4$
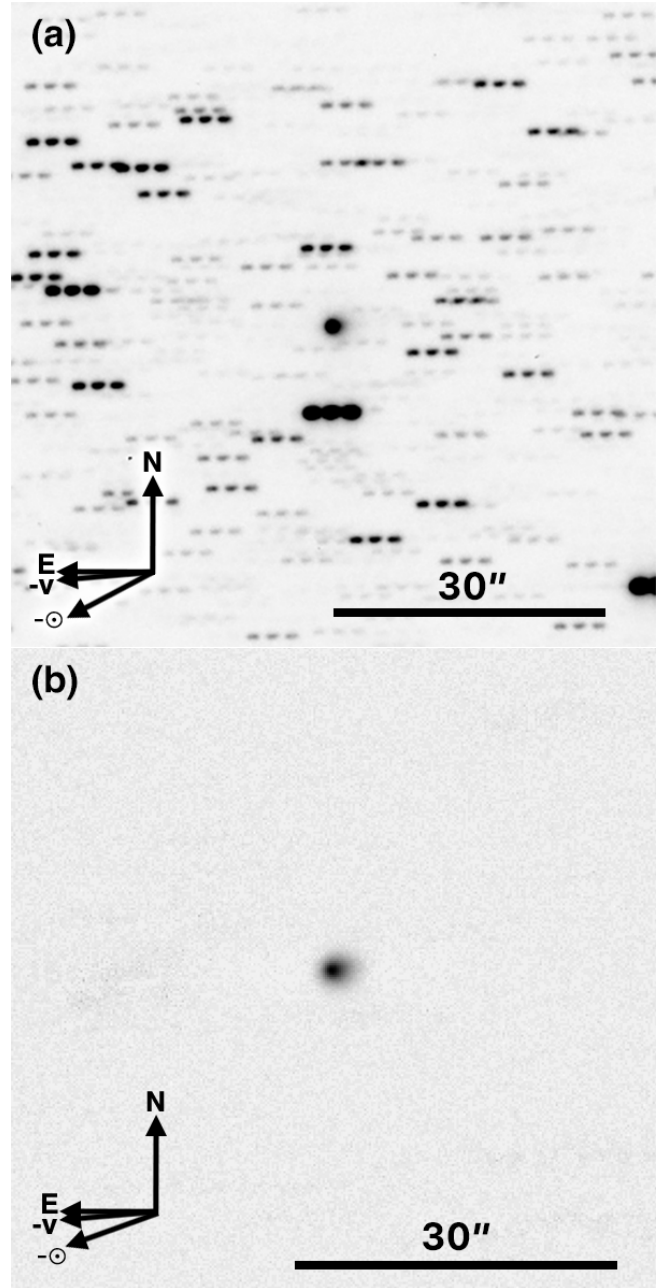
Figure 3. (a) Stacked gri-band image cut-out from CFHT on 2025 July 2 and (b) R-band composite image from VLT on 2025 July 4, both showing faint activity. Background objects were removed from the VLT stack. Arrows indicate the directions of North (N), East (E), the anti-solar vector as projected on the sky ($-\odot$), and the negative heliocentric velocity vector as projected on the sky ($-v$).

and a standard deviation of 0.07 mag. The photometry from 2025 June 18 (the last night plotted in Figure 5 when the object was at $r = 4.9$ au) corresponds to an absolute magnitude outside that standard deviation at $H_V = 12.1$. For comparison, r'-band light curve data obtained from LCO-network telescopes (discussed
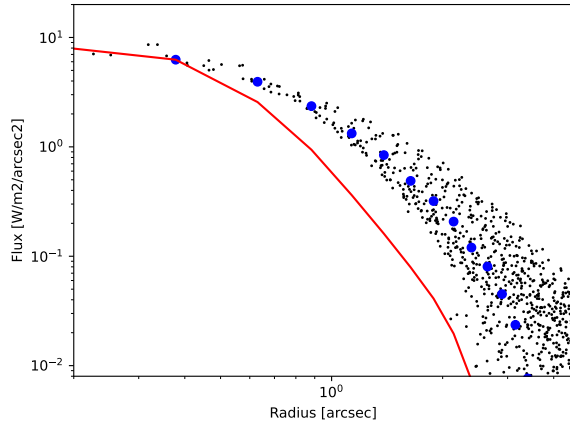
Figure 4. Photometric profile of the VLT image (Figure 3a). The individual pixels are represented by black dots; average in annuli by blue circles. The red line is the average stellar profile measured on 10 nearby well-exposed stars.
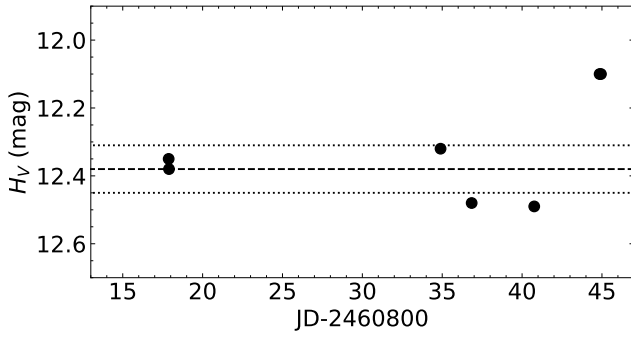
Figure 5. Absolute magnitudes computed from ZTF pre-covery data published in MPEC 2025-N51 from 2025 May 22 to June 18. The median H_V and standard deviation of data are shown by a dashed horizontal line and dotted horizontal lines, respectively. No photometric uncertainties were reported for these data.

in more detail in Section 3.2) show an approximate average r'-band apparent magnitude of $m_r \sim 17.9$, corresponding to $H_V = 11.9$, indicating that the faint coma visible in CFHT and VLT data obtained on 2025 July 2 and 4 could be responsible for about 0.5 mag of excess brightening of the object since early June.

We note that this finding does not exclude the presence of coma prior to mid-June, but indicates that any coma that may have been present was relatively steady-state from late May to early June, and then increased in mid-June. For reference, $H_V = 12.4$ corresponds to a radius of 10–11 km for an albedo of 0.04–0.05 typical of comets, but this is an upper limit given that we cannot rule out activity during the observations used to derive this result.

3.2. *Rotation*

In order to characterize 3I/ATLAS's rotational light curve, we obtained time-series observations between 2025 July 2 and July 4 using two separate 0.35-meter telescopes from the LCO Haleakala observatory (MPC codes T03, T04), the 2.0-meter Faulkes Telescope North (FTN, MPC code F65) at Haleakala Observatory, and the 2.0-meter Faulkes Telescope South (FTS, MPC code E10) at Siding Spring Observatory, all of which are part of the same network. Time-series observations were also obtained on 2025 July 4–5 using the Telescope Joan Oró (TJO, MPC code C65) at Montsec Observatory.

Photometric observations were obtained on the nights of 2025 July 2–4 with the TRAPPIST telescopes (Jehin et al. 2011). TRAPPIST-South (TS, MPC code I40) is located at the ESO La Silla Observatory in Chile, and TRAPPIST-North (TN, MPC code Z53) is located at the Oukaimeden observatory in Morocco. Both telescopes are 0.6-meter Ritchey-Chretien telescopes operating at f/8. TS is equipped with a FLI ProLine 3041-BB CCD camera with a 22$'$ field of view and a pixel scale of 0$\farcs$64 pixel^{-1}. The TN camera is an Andor IKONL BEX2 DD camera providing a 20$'$ field of view and pixel scale of 0$\farcs$60 pixel^{-1}. Johnson-Cousin R_c filters were used with 2×2 binning (1$\farcs$2 pixel^{-1}) and an exposure time of 180 s. Photometry was performed with the PHOTOMETRYPIPELINE (Mommert 2017a) by matching ~100 field stars in each image with the Pan-STARRS DR1 photometric catalog and using an aperture radius of 4 pixels.

We also obtained time-series observations of 3I/ATLAS in o-band (AB; approximately equivalent to $r' + i'$) using the ATLAS network starting at ~23:00 UTC on 2025 July 4, interleaving 3I/ATLAS exposures approximately every four of normal survey operations. Using the ATLAS sites in Chile and Haleakala (ATLAS-HKO and ATLAS-CHL; MPC codes W68 and T05), a 13 h continuous light curve was obtained from the normal differencing pipeline. The zeropoint for each exposure is derived from $\sim 10^5$ reference stars from Refcat2 (Tonry et al. 2018b).

Compiled light curve results are shown in Figure 6. Apart from the differences produced by the variety of filters used, offsets between datasets are likely due to background stars and differences in pipeline removal processes. No periodicity is immediately apparent within any of the datasets, indicating little brightness variation during the observation period. This is in notable contrast to 1I/'Oumuamua, which displayed a far more extreme light curve range of ~ 3.5 magnitudes (see Section 1). It should be noted, however, that the detection of activity and coma (Section 3.1) means that any photo-
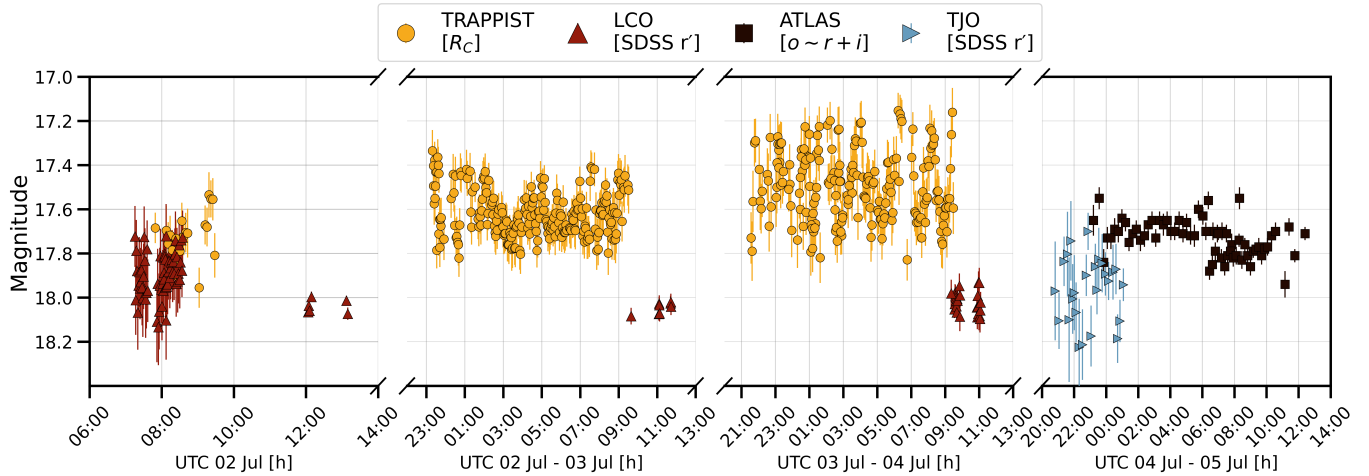
Figure 6. Compiled light curve of 3I/ATLAS incorporating r'-band data from the LCO 0.35-meter telescopes, Faulkes Telescope North, Faulkes Telescope South, and the Telescope Joan Oró, Johnson-Cousins Rc-band data from the TRAPPIST-North and -South telescopes, and o-band data from ATLAS-HKO and ATLAS-CHL.

metric variations caused by a rotating nucleus will be at least partially suppressed by the relatively more steady state coma surrounding it.

We note that accurate photometry of much of our time series data was impacted by background source interference as 3I/ATLAS passes through the Galactic plane. Additional follow-up observations of 3I/ATLAS once it leaves the Galactic plane region of the sky and its background fields become less crowded will constrain the rotation period.

3.3. *Colors*

Two multi-filter imaging sequences were obtained with the 2.0-meter Faulkes Telescope North on Haleakala using the four-channel MuSCAT3 imager, which records the Sloan g'-, r'-, i'-, and z_s-bands simultaneously: (i) six exposures of 30 s in each filter, and (ii) three exposures of 50 s in each filter, yielding total integrations of 180 s and 150 s per band, respectively. The data output by the LCO reduction pipelines were processed with PHOTOMETRYPIPELINE (Mommert 2017b), which performs SCAMP astrometric solutions against *Gaia* DR3 (Gaia Collaboration et al. 2023) and aperture photometry calibrated to Pan-STARRS DR2 (Flewelling et al. 2020).

In Figure 7, we show the resulting four-color surface reflectance spectrum of the object from the FTN.

The colors of 3I/ATLAS as seen in Figure 7 are relatively linear (e.g., without obvious absorption features or spectral curvature) and significantly redder than those of the Sun. This reflectance spectrum is approximately 18 %/100 nm as derived from the full range of the available color data. It is similar, though somewhat redder, to that retrieved for 1I/'Oumuamua (10±6 %/100
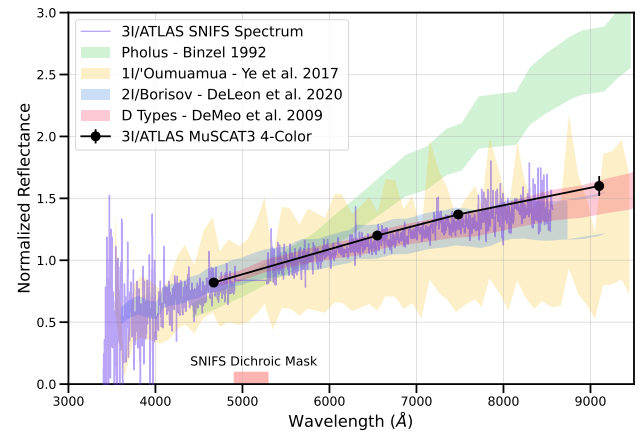
Figure 7. The g',r',i',z' colors of 3I/ATLAS obtained with FTN as well as the reflectance spectrum obtained with SNIFS on the UH 2.2-meter at Maunakea normalized at 5500 Å and plotted against 1I/'Oumuamua (Ye et al. 2017), 2I/Borisov (de León et al. 2020), the extremely red Centaur Pholus (Binzel 1992), and the mean D-type asteroid spectrum (DeMeo et al. 2009). Note that errors on the color measurement are plotted, but are approximately the size of the plot points. The region of the spectrum masked due to the SNIFS dichroic sensitivity is highlighted in red. Both the observed spectrum and the four-color derived reflectance slopes are in agreement. 3I/ATLAS shows a moderately red spectral slope similar to 1I/'Oumuamua and 2I/Borisov.

nm, Ye et al. 2017) and 2I/Borisov (12±1 %/100 de León et al. 2020), both of which are slightly redder than the D-type asteroids (DeMeo et al. 2009). However, it is not as red as seen in some outer Solar System objects (e.g. Pholus, Binzel 1992). Some of the reflected light must be from the coma because 3I/ATLAS is weakly active. This is corroborated by the fact that photome-

try of g'- and r'-band ZTF precovery data (Section 3.1) obtained when the object appeared to be less active, indicated that the $g' - r'$ colors on those nights were extremely close to solar. Specifically, the measurements were $(g' - r') = 0.42$ on 2025 May 22 and $(g' - r') = 0.44$ on June 18, compared to $(g' - r')_\odot = 0.45$ (Holmberg et al. 2006). This suggests that the much redder color measured from later data could be heavily affected by ejected dust. The spectral slope measured here is slightly higher than the average for cometary dust (see modeling and discussions of typical Solar System comets in Protopapa et al. 2018; Kareta et al. 2023, as well as Figure 3 of Kolokolova et al. 2024), but not significantly so. 2I/Borisov's coma was similarly red (see, e.g., de León et al. 2020), but the object was also significantly more active at the time of the color observations.

3.4. *Spectrum*

The spectrum shown in Figure 7 was obtained on 2025 July 4 using the SNIFS instrument (SuperNova Integral Field Spectrograph; Lantz et al. 2004) on the UH 2.2-meter telescope at Maunakea by the Spectroscopic Classification of Astronomical Transients (SCAT; Tucker et al. 2022) team. Data reduction followed the procedures described in Tucker et al. (2022). SNIFS contains two channels split by a dichroic mirror, with a blue channel covering 0.34–0.51 μm, and a red channel covering 0.51–1.0 μm, with spectral resolutions of 5 Å and 7 Å, respectively. The fast reduction pipeline used here does not include the full dichroic correction; therefore, data in this region were excluded from the final spectrum. In addition to 3I/ATLAS, the solar analog HD 165290 was observed. The final calibrated reflectance spectrum obtained by dividing the target spectrum by the normalized spectrum of the solar analog is shown in Figure 7.

The normalized reflection spectrum shows no obvious absorption features or gas emissions and yields a spectral slope of 17.1±0.2 %/100 nm. This value was determined with a linear fitting routine with bootstrapping to estimate uncertainties. This spectral slope confirms the moderately red slope observed with the MuSCAT3 images, further solidifying a color similarity to both D-types and 2I/Borisov.

4. DISCUSSION

Given that three interstellar objects have now been discovered, it is worthwhile to use their measured physical properties and discovery circumstances to estimate the size of the total population in the Solar System.

The volume within which ATLAS can detect a moving object depends strongly on intrinsic brightness (H_V)
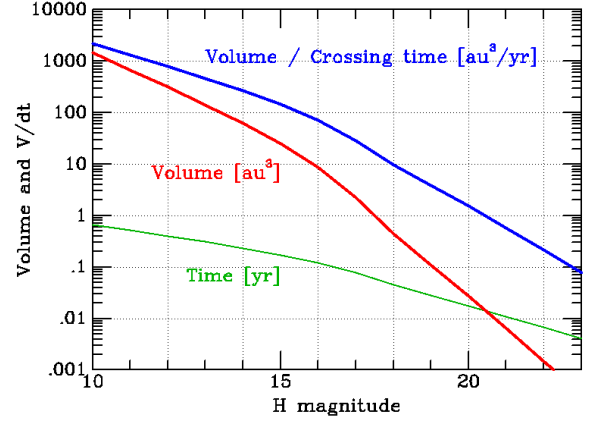
Figure 8. The volume in which ATLAS can detect an object is plotted as a function of H magnitude (red). The ratio of volume and crossing time (blue) is approximately the product of detection cross section and velocity. When the visibility time (green) becomes less than ~ 0.1 yr (a lunation) weather and other effects will diminish the chances of a detection below the V/dt curve.

and location in the Solar System, where sensitivity, illumination, distance, phase function, and trailing losses are critical components. Using an ATLAS detection model that assumes a $G = 0.15$ phase function, a speed of 50 km s^{-1} for trailing losses, a weather and moon averaged limiting $m_{lim} \simeq 19$, and 50 km s^{-1} speed for volume crossing, Figure 8 shows the volume in which ATLAS can detect an object.

This curve of detectability volume divided by crossing time has a slope of $\log(V/dt) \propto -0.2 H_V$ for $H_V < 15$ and a slope of $\log(V/dt) \propto -0.4 H_V$ for $H_V > 15$. However, the crossing time for $H > 16$ is less than 0.1 yr which means that the actual detectability is certainly less than V/dt from Figure 8 because of weather and other survey cadence effects. The ratio of detectability volume and crossing time is approximately the product of detection cross section and velocity, hence the ratio of detection rate and local density. Evaluating Figure 8 at $H_V \sim 12.5$ for 3I/ATLAS gives 600 au^3 yr^{-1}, and a local density of $\sim 3 \times 10^{-4}$ au^{-3} for a detection rate of ~ 0.2 yr^{-1}.

The $G = 0.15$ phase function used for Figure 8 may be inappropriate for an object such as 3I/ATLAS with an unknown amount of coma, and unknown and potentially unfamiliar surface scattering properties, which could cause this density estimate to be significantly incorrect. Obtaining stronger constraints on 3I/ATLAS's nucleus size, such as with high-resolution imaging by space telescopes or adaptive optics-equipped ground-based telescopes, or by searching for occultation obser-

vation opportunities, should therefore be considered a high priority.

Do et al. (2018) estimated an interstellar density of objects like 1I/'Oumuamua at 0.2 au^{-3} ($H_V \sim 23$) and noted that the size distribution must be steeper than $n(d > D) \propto D^{-3}$ to avoid a logarithmic divergence in total mass, i.e. differential $\log n(d)$ with slope greater than $0.8 H_V$ (see Fig. 3 of Do et al. 2018). This criterion applied to the ATLAS detectability curve would cause a strong peak around $H \sim 16$, not two detections at $H \sim 13$, however. As such, the detections of 2I/Borisov and 3I/ATLAS, both of which appear, or appeared, relatively large, are somewhat unexpected given that more numerous smaller interstellar objects have not also been discovered over the same time period. Clearly what is needed is more interstellar object discoveries to improve population statistics, which is hopefully exactly what the Rubin Observatory Legacy Survey of Space and Time (LSST; Jones et al. 2009) will deliver in the coming years.

We are certain to learn more about 3I/ATLAS in the coming weeks and months as it experiences continued and increasing heating for perhaps the first time during its passage past our Sun. Comprehensive and collaborative investigations of 3I/ATLAS based off the lessons learned from the 1I/'Oumuamua and 2I/Borisov campaigns are poised to significantly expand our knowledge of the interstellar object population, and as such, additional observations of 3I/ATLAS are highly encouraged. Further photometry, spectroscopy, or polarimetry could constrain the rotation, activity, dust size-frequency distribution, coma composition, and nongravitational acceleration of the object. The perihelion of 3I/ATLAS will not be easily observable from Earth-based observatories, as the object will be on the opposite side of the Sun and at a low solar elongation angle. However, the object will approach within 0.19 au of Mars, and we encourage nearby spacecraft (e.g., Mars Reconnaissance Orbiter, Trace Gas Orbiter, MAVEN, Tianwen-1, Hope, Jupiter Icy Moons Explorer) equipped with visible, UV, and IR spectrographs and cameras to attempt to capture data on this object's closest approach.

AUTHOR CONTRIBUTIONS

Facility: Las Cumbres Observatory; Canada-France-Hawaii Telescope; Very Large Array; ATLAS; Zwicky Transient Facility; ESA Test Bed Telescopes

Software:

REFERENCES

Almeida-Fernandes, F., & Rocha-Pinto, H. J. 2018, MNRAS, 480, 4903, doi: 10.1093/mnras/sty2202

Aravind, K., Ganesh, S., Venkataramani, K., et al. 2021, MNRAS, 502, 3491, doi: 10.1093/mnras/stab084

Bagnulo, S., Cellino, A., Kolokolova, L., et al. 2021, Nature Communications, 12, 1797,

doi: 10.1038/s41467-021-22000-x

Bannister, M. T., Opitom, C., Fitzsimmons, A., et al. 2020, arXiv e-prints, arXiv:2001.11605. https://arxiv.org/abs/2001.11605

Bellm, E. C., Kulkarni, S. R., Graham, M. J., et al. 2019, PASP, 131, 018002, doi: 10.1088/1538-3873/aaecbe

Belton, M. J. S., Hainaut, O. R., Meech, K. J., et al. 2018, ApJL, 856, L21, doi: 10.3847/2041-8213/aab370

Bergner, J. B., & Seligman, D. Z. 2023, Nature, 615, 610, doi: 10.1038/s41586-022-05687-w

Binzel, R. P. 1992, Icarus, 99, 238, doi: 10.1016/0019-1035(92)90185-A

Biver, N., Dello Russo, N., Opitom, C., & Rubin, M. 2024, in Comets III, ed. K. J. Meech, M. R. Combi, D. Bockelée-Morvan, S. N. Raymodn, & M. E. Zolensky (University of Arizona Press), 459–498

Bodewits, D., Noonan, J. W., Feldman, P. D., et al. 2020, Nature Astronomy, 4, 867, doi: 10.1038/s41550-020-1095-2

Bolin, B. T., Weaver, H. A., Fernandez, Y. R., et al. 2018, ApJL, 852, L2, doi: 10.3847/2041-8213/aaa0c9

Bolin, B. T., Lisse, C. M., Kasliwal, M. M., et al. 2020, AJ, 160, 26, doi: 10.3847/1538-3881/ab9305

Borisov, G., Durig, D. T., Sato, H., et al. 2019, Central Bureau Electronic Telegrams, 4666, 1

Boulade, O., Charlot, X., Abbon, P., et al. 2003, in Proc. SPIE, Vol. 4841, Instrument Design and Performance for Optical/Infrared Ground-based Telescopes, 72–81, doi: 10.1117/12.459890

Bowell, E., Hapke, B., Domingue, D., et al. 1989, in Asteroids II, 524–556

Cordiner, M. A., Milam, S. N., Biver, N., et al. 2020, Nature Astronomy, 4, 861, doi: 10.1038/s41550-020-1087-2

Cremonese, G., Fulle, M., Cambianica, P., et al. 2020, ApJL, 893, L12, doi: 10.3847/2041-8213/ab8455

de León, J., Licandro, J., de la Fuente Marcos, C., et al. 2020, MNRAS, 495, 2053, doi: 10.1093/mnras/staa1190

DeMeo, F. E., Binzel, R. P., Slivan, S. M., & Bus, S. J. 2009, Icarus, 202, 160, doi: 10.1016/j.icarus.2009.02.005

Desch, S. J., & Jackson, A. P. 2021, Journal of Geophysical Research: Planets, e2020JE006807

Desch, S. J., & Jackson, A. P. 2022, Astrobiology, 22, 1400, doi: 10.1089/ast.2021.0199

Do, A., Tucker, M. A., & Tonry, J. 2018, ApJL, 855, L10, doi: 10.3847/2041-8213/aaae67

Farnocchia, D., Seligman, D. Z., Granvik, M., et al. 2023, PSJ, 4, 29, doi: 10.3847/PSJ/acb25b

Feng, F., & Jones, H. R. A. 2018, ApJL, 852, L27, doi: 10.3847/2041-8213/aaa404

Fitzsimmons, A., Meech, K., Matrà, L., & Pfalzner, S. 2024, in Comets III, ed. K. J. Meech, M. R. Combi, D. Bockelée-Morvan, S. N. Raymodn, & M. E. Zolensky, 731–766

Fitzsimmons, A., Snodgrass, C., Rozitis, B., et al. 2018, Nature Astronomy, 2, 133, doi: 10.1038/s41550-017-0361-4

Fitzsimmons, A., Hainaut, O., Meech, K. J., et al. 2019, ApJL, 885, L9, doi: 10.3847/2041-8213/ab49fc

Flekkøy, E. G., Luu, J., & Toussaint, R. 2019, ApJL, 885, L41, doi: 10.3847/2041-8213/ab4f78

Flewelling, H. A., Magnier, E. A., Chambers, K. C., et al. 2020, ApJS, 251, 7, doi: 10.3847/1538-4365/abb82d

Fraser, W. C., Pravec, P., Fitzsimmons, A., et al. 2018, Nature Astronomy, 2, 383, doi: 10.1038/s41550-018-0398-z

Gaia Collaboration, Vallenari, A., Brown, A. G. A., et al. 2023, A&A, 674, A1, doi: 10.1051/0004-6361/202243940

Gaidos, E., Williams, J., & Kraus, A. 2017, RNAAS, 1, 13, doi: 10.3847/2515-5172/aa9851

Graham, M. J., Kulkarni, S. R., Bellm, E. C., et al. 2019, PASP, 131, 078001, doi: 10.1088/1538-3873/ab006c

Guzik, P., Drahus, M., Rusek, K., et al. 2020, Nature Astronomy, 4, 53, doi: 10.1038/s41550-019-0931-8

Hallatt, T., & Wiegert, P. 2020, AJ, 159, 147

Holmberg, J., Flynn, C., & Portinari, L. 2006, MNRAS, 367, 449, doi: 10.1111/j.1365-2966.2005.09832.x

Hsieh, C.-H., Laughlin, G., & Arce, H. G. 2021, ApJ, 917, 20, doi: 10.3847/1538-4357/ac0729

Hui, M.-T., Ye, Q.-Z., Föhring, D., Hung, D., & Tholen, D. J. 2020, AJ, 160, 92, doi: 10.3847/1538-3881/ab9df8

Jackson, A. P., & Desch, S. J. 2021, Journal of Geophysical Research: Planets, e2020JE006706

Jehin, E., Gillon, M., Queloz, D., et al. 2011, The Messenger, 145

Jewitt, D., & Luu, J. 2019, ApJL, 886, L29, doi: 10.3847/2041-8213/ab530b

Jewitt, D., Luu, J., Rajagopal, J., et al. 2017, ApJL, 850, L36, doi: 10.3847/2041-8213/aa9b2f

Jewitt, D., & Seligman, D. Z. 2023, ARA&A, 61, 197, doi: 10.1146/annurev-astro-071221-054221

Jones, R. L., Chesley, S. R., Connolly, A. J., et al. 2009, Earth Moon and Planets, 105, 101, doi: 10.1007/s11038-009-9305-z

Jordi, K., Grebel, E. K., & Ammon, K. 2006, A&A, 460, 339, doi: 10.1051/0004-6361:20066082

Kareta, T., Noonan, J. W., Harris, W. M., & Springmann, A. 2023, PSJ, 4, 85, doi: 10.3847/PSJ/accc28

Kareta, T., Andrews, J., Noonan, J. W., et al. 2020, ApJL, 889, L38, doi: 10.3847/2041-8213/ab6a08

Kim, Y., Jewitt, D., Mutchler, M., et al. 2020, ApJL, 895, L34, doi: 10.3847/2041-8213/ab9228

Knight, M. M., Protopapa, S., Kelley, M. S. P., et al. 2017, ApJL, 851, L31, doi: 10.3847/2041-8213/aa9d81

Kolokolova, L., Kelley, M. S. P., Kimura, H., & Hoang, T. 2024, in Comets III, ed. K. J. Meech, M. R. Combi, D. Bockelée-Morvan, S. N. Raymodn, & M. E. Zolensky (University of Arizona Press), 621–652

Lantz, B., Aldering, G., Antilogus, P., et al. 2004, in Society of Photo-Optical Instrumentation Engineers (SPIE) Conference Series, Vol. 5249, Optical Design and Engineering, ed. L. Mazuray, P. J. Rogers, & R. Wartmann, 146–155, doi: 10.1117/12.512493

Levine, W. G., Cabot, S. H. C., Seligman, D., & Laughlin, G. 2021, ApJ, 922, 39, doi: 10.3847/1538-4357/ac1fe6

Levine, W. G., & Laughlin, G. 2021, ApJ, 912, 3, doi: 10.3847/1538-4357/abec85

Lin, H. W., Lee, C.-H., Gerdes, D. W., et al. 2020, ApJL, 889, L30, doi: 10.3847/2041-8213/ab6bd9

Lister, T., Kelley, M. S. P., Holt, C. E., et al. 2022, PSJ, 3, 173, doi: 10.3847/PSJ/ac7a31

Luu, J. X., Flekkøy, E. G., & Toussaint, R. 2020, ApJL, 900, L22, doi: 10.3847/2041-8213/abafa7

Mamajek, E. 2017, Research Notes of the American Astronomical Society, 1, 21, doi: 10.3847/2515-5172/aa9bdc

Mashchenko, S. 2019, MNRAS, 489, 3003, doi: 10.1093/mnras/stz2380

McKay, A. J., Cochran, A. L., Dello Russo, N., & DiSanti, M. A. 2020, ApJL, 889, L10, doi: 10.3847/2041-8213/ab64ed

Meech, K. J., Weryk, R., Micheli, M., et al. 2017, Nature, 552, 378, doi: 10.1038/nature25020

Micheli, M., Farnocchia, D., Meech, K. J., et al. 2018, Nature, 559, 223, doi: 10.1038/s41586-018-0254-4

Mommert, M. 2017a, Astronomy and Computing, 18, 47

—. 2017b, Astronomy and Computing, 18, 47

Moro-Martín, A. 2019, ApJL, 872, L32

Moro-Martín, A. 2022, arXiv e-prints, arXiv:2205.04277, doi: 10.48550/arXiv.2205.04277

Opitom, C., Fitzsimmons, A., Jehin, E., et al. 2019, A&A, 631, L8, doi: 10.1051/0004-6361/201936959

Protopapa, S., Kelley, M. S. P., Yang, B., et al. 2018, ApJL, 862, L16, doi: 10.3847/2041-8213/aad33b

Sekanina, Z. 2019, arXiv e-prints, arXiv:1905.00935. https://arxiv.org/abs/1905.00935

Seligman, D., & Laughlin, G. 2020, ApJL, 896, L8, doi: 10.3847/2041-8213/ab963f

Seligman, D. Z., & Moro-Martín, A. 2023, Contemporary Physics, 63, 200, doi: 10.1080/00107514.2023.2203976

Seligman, D. Z., Farnocchia, D., Micheli, M., et al. 2023, PSJ, 4, 35, doi: 10.3847/PSJ/acb697

—. 2024, Proceedings of the National Academy of Science, 121, e2406424121, doi: 10.1073/pnas.2406424121

Taylor, A. G., Seligman, D. Z., Hainaut, O. R., & Meech, K. J. 2023, PSJ, 4, 186, doi: 10.3847/PSJ/acf617

Taylor, A. G., Steckloff, J. K., Seligman, D. Z., et al. 2024, Icarus, 420, 116207, doi: 10.1016/j.icarus.2024.116207

Tonry, J. L., Denneau, L., Heinze, A. N., et al. 2018a, PASP, 130, 064505, doi: 10.1088/1538-3873/aabadf

Tonry, J. L., Denneau, L., Flewelling, H., et al. 2018b, ApJ, 867, 105, doi: 10.3847/1538-4357/aae386

Trilling, D. E., Mommert, M., Hora, J. L., et al. 2018, AJ, 156, 261

Tucker, M. A., Shappee, B. J., Huber, M. E., et al. 2022, PASP, 134, 124502, doi: 10.1088/1538-3873/aca719

Williams, G. V., Sato, H., Sarneczky, K., et al. 2017, Central Bureau Electronic Telegrams, 4450, 1

Xing, Z., Bodewits, D., Noonan, J., & Bannister, M. T. 2020, ApJL, 893, L48, doi: 10.3847/2041-8213/ab86be

Yang, B., Li, A., Cordiner, M. A., et al. 2021, Nature Astronomy, doi: 10.1038/s41550-021-01336-w

Ye, Q., Kelley, M. S. P., Bolin, B. T., et al. 2020, AJ, 159, 77, doi: 10.3847/1538-3881/ab659b

Ye, Q.-Z., Zhang, Q., Kelley, M. S. P., & Brown, P. G. 2017, ApJL, 851, L5, doi: 10.3847/2041-8213/aa9a34